Observations of Quasi-Stationary and Shallow Orographic Snow Clouds: Spatial Distributions of Supercooled Liquid Water and Snow Particles

KENICHI KUSUNOKI, MASATAKA MURAKAMI, NARIHIRO ORIKASA, MIZUHO HOSHIMOTO, AND YOSHINOBU TANAKA

Meteorological Research Institute, Tsukuba, Japan

YOSHINORI YAMADA

Japan Meteorological Agency, Tokyo, Japan

HAKARU MIZUNO

Meteorological College, Kashiwa, Japan

KYOSUKE HAMAZU

Mitsubishi Electric Corporation, Tokyo, Japan

HIDEYUKI WATANABE

Tone River Dams Integrated Control Office, Ministry of Land, Infrastructure, and Transport, Maebashi, Japan

(Manuscript submitted 22 January 2004, in final form 3 August 2004)

ABSTRACT

On 25 February 1999, due to a winter monsoon after a cyclonic storm, orographic snow clouds formed under conditions of weak cold advection on the western side of the central mountain range of Japan. In this study, the Ka-band Doppler radar and vehicle-mounted microwave radiometer and 2D-Grey imaging probe were used to obtain unique datasets for analyzing the spatial distributions of microphysical structures of the snow clouds at the windward slope. The liquid water path, number concentration of snow particles (0.1–6.4 mm diameter), and precipitation rate were found to be correlated with altitude. The greater concentration of larger particles tended to appear up the slope. The echo top was at about 2.5 km (-30 dBZ), and the relatively strong echo region (>-3 dBZ) appeared at 5 km up the slope and extended nearly parallel to the slope. According to the echo pattern, the ice water path increased with terrain height and reached the maximum intensity at about 14 km up the slope. These observations provide indirect evidence that terrain-induced updrafts lead to the generation and growth of supercooled cloud droplets and indicate that the riming process plays an important role in the growth of snow particles at higher altitudes. In this paper, it is confirmed that the abundance of supercooled liquid water (SLW) during intensified monsoon flow is due to larger water production rates caused by higher vertical velocities induced by topography. Furthermore, it can be shown that small-scale terrains enhance localized updrafts embedded within the larger-scale flow and have noticeable impact on SLW cloud distribution.

1. Introduction

This paper is the second in a series describing the 25 February 1999 shallow orographic precipitating clouds over the Mikuni Mountains of Japan. In the previous paper, Kusunoki et al. (2004, hereafter KM04) summarized the temporal evolution of the meso- and microscale structures as well as environmental conditions associated with variations in thermodynamic stratification and kinematic motion. These results are important for the technology of scientific weather modification over the Japan Sea area, which depends critically on the understanding of physical processes associated with the formation and evolution of ice and supercooled liquid water (SLW) under winter monsoons. It has been found in KM04 that the presence of SLW in clouds resulting from the intensified monsoon flow is one of

Corresponding author address: Kenichi Kusunoki, Meteorological Research Institute, Japan Meteorological Agency, 1-1 Nagamine, Tsukuba, Japan.
E-mail: kkusunok@mri-jma.go.jp

criteria to be used for determining the storm modification potential. Enhanced flow up the slope results in strong upward air motion and production of SLW. In particular, the clouds between 1700 and 2200 UTC (i.e., stage II in KM04) showed an abundance of SLW. UTC equals Japan Standard Time (JST) plus 9 h. In this study, the spatial distribution of microphysical parameters within the upslope zone during an orographic snow event is examined. This allows the connection between the wind speed up the slope and the SLW to be clarified. The main instruments on the mobile platform used for this study were the microwave radiometer and optical imaging probe (2D-Grey), providing a unique dataset of precipitation particles (e.g., size spectra and shape) as well as liquid water. The spatial distributions of microphysical properties are described in this paper by combining the data from both the vehicle-mounted instruments and Ka-band Doppler radar.

In section 2, the instruments used in our experiments are described. The distributions of supercooled liquid water and snow particles are analyzed in section 3, followed by the summary and conclusions in section 4.

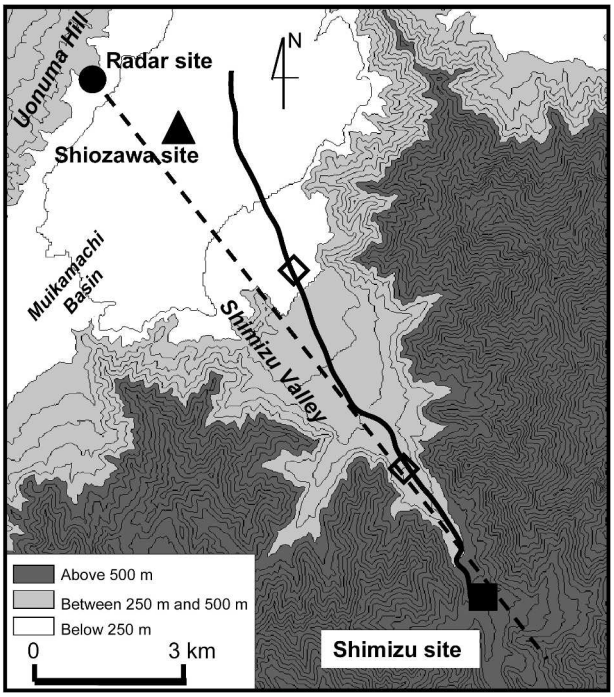

FIG. 1. Topographical map around the study area including geographic names. The locations marked by the symbols are as follows: the site of the Ka-band Doppler radar on the Uonuma Hill (circle); rawinsonde soundings were operated at the Shiozawa site (triangle); the stationary microwave radiometer at the Shimizu site (square). The bold line indicates the route of mobile measurements. The radar RHI scan was at the azimuth angle of 141° consistent with the valley axis (dashed line). The locations of bottlenecks are marked by diamonds (see section 3). Terrain contours are at 50-m intervals, with darker shadings representing higher elevations.

2. Instrumentation

The instruments used in this study include 1) a mobile platform and 2) a Ka-band Doppler radar. In addition to the above instruments, rawinsondes were launched at 1737 and 1856 UTC from the Shiozawa site. Figure 1 shows the locations of the ground-based instruments deployed along the Shimizu Valley. More details on the features of the terrain of the study area are given by KM04. The airflow of monsoons from the Sea of Japan, which blow nearly parallel to the valley axis, converge and rise at the windward side as a result of the local orography of the valley. Such orographically modified flows develop shallow but vigorous snow clouds in a favorable thermodynamic environment already destabilized by passage over the warm Sea of Japan. The deployment of instruments and the route of mobile measurements along the Shimizu Valley are suitable for our primary interest, which is the local occurrences of SLW and snow, and thus, the nature of the orographically enhanced modifications in snow clouds.

a. The mobile platform

While the cloud structure and particle distributions have been already extensively studied by remote sensing techniques, cloud microphysical properties can be measured primarily with in situ airborne instrumentation (e.g., Cooper and Saunders 1980; Heggli et al. 1983; Rauber and Grant 1986; Murakami et al. 2000). Aircraft in situ observations, on the other hand, are generally costly, sometimes require long time intervals between data acquisition periods, and are limited in that they cannot be made very close to mountainous terrain. Therefore, in order to investigate quasi-stationary orographic snow clouds, ground-based mobile instruments are more appropriate. Such clouds are usually not observed exactly in situ but from a close distance with vehicle-mounted instruments. The concept of mobile observations of orographic snow clouds is not entirely new. Holroyd (1986) and Deshler (1988) developed and used a truckborne 2D-C probe for winter orographic clouds in the Sierra Nevadas and in Colorado. The Desert Research Institute (DRI) in Nevada, has developed a dual-frequency mobile microwave radiometer (MMR), which is a vehicle-mounted microwave radiometer used for estimating column-integrated water vapor and cloud liquid water from a moving vehicle (Huggins 1995).

The mobile platform in this study was equipped with a 2D-Grey imaging probe, a microwave radiometer, conventional sensors (thermometer, hygrometer, and anemometer), and a global positioning system (GPS) receiver, which measured the vehicle position, heading, and speed (Fig. 2). Wind direction and speed relative to the ground were derived using the vehicle heading and speed from the GPS together with the vehicle-relative wind direction and speed from the anemometer in-

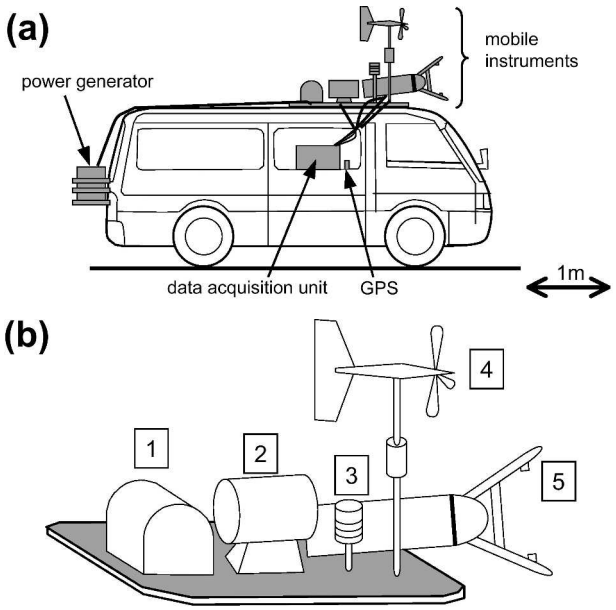

FIG. 2. (a) Schematic of the mobile platform. (b) Rooftop layout, including (1) microwave radiometer, (2) air blower for removing raindrops and snow from the radiometer radome, (3) thermister and hygrometer, (4) anemometer, and (5) 2D-Grey imaging probe.

stalled on the vehicle. The data acquisition and storage system, as well as the real-time display units, were housed in the vehicle. A gasoline-fueled power generator was installed at the rear of the vehicle to provide electric power to these instruments. The integration time of the microwave radiometer was 1 min, whereas that for other measurements had a duration of 1 s. The horizontal resolution depended on the vehicle speed. For example, 30 km h^{-1} and 1 min of data corresponded to approximately 500 m, and 1 s of data corresponded to 8 m of horizontal distance. The route of mobile measurements is shown by the bold line in Fig. 1. In this study, the vehicle made four round trips between near the Shiozawa site (a height of 190 m) and the Shimizu site (a height of 580 m). Each round took about 25 min.

1) THE 2D-GREY IMAGING PROBE

The 2D-Grey imaging probe belongs to the Particle Measuring Systems (PMS) family of optical array probes, which are the main in situ instruments used for cloud particle measurements in airborne studies (Knollenberg 1970). As particles cross the laser beam within the depth of field (DOF), they cast a shadow onto the photodiode array, causing the light levels to be reduced below some threshold of laser intensity. The array produces two-dimensional image slices at a frequency that is proportional to the true air speed (TAS), which is derived from the anemometer data and vehicle heading vector from the GPS. The probe, which was mounted on the front of the vehicle roof, measured the spatial distribution of particle sizes (0.1–6.4 mm diameter), shapes, and concentration of precipitation particles along the route. The 2D-Grey imaging probe allows us to distinguish four shadow (gray) levels, corresponding to thresholds at 75%, 50%, and 25% of laser intensity. In this study, only the 50% threshold level was used. Particle images were sized by the diameter of equivalent circles, that is, the diameter of a circle with the same area as the particle. Heymsfield and Parrish's (1978) equation for sampling area, which takes into account particles on the edges of the array, was then utilized for calculating concentration. Zero-area images were assumed to be negligible because the TAS was very small (i.e., 17 m s^{-1} or less) in terms of the maximum slice rate of 4 MHz. Blank images caused by very small particles that might have been present were not accounted for because of the lack of a reliable method for incorporating them. Streakers or other artifacts were not found by visual inspection. Even if some misidentifications remain, they can be expected to be mitigated by the averaging process. Other errors may be introduced by blowing snow from the road or the side of the road, but we assumed the impact to be negligible because the surface wind was so weak (Li and Pomeroy 1997).

2) MOBILE MICROWAVE RADIOMETER

(i) Instrument overview

The microwave radiometer is a useful tool for studies of SLW in snow clouds. In this work, dual-frequency (23.8 and 31.4 GHz) passive microwave radiometers (WVR-1100; Radiometrics 1997) were used. Brightness temperatures, which the microwave radiometer measures at both frequencies, are used to estimate vertically integrated water vapor and liquid water content (LWC) [or liquid water path (LWP)], as described by Hogg et al. (1983). In this study, a microwave radiometer mounted on the roof of the vehicle was operated in the zenith-pointing mode and used for observing the spatial distributions of the LWP along the valley. Data on the water vapor path were not used in this study. A stationary microwave radiometer was operated at the Shimizu site, but its dataset was used only for the purpose of comparison with the LWP data of the mobile radiometer (see next subsection).

(ii) LWP data quality checking

The surface temperatures observed with the mobile platform in the study period were slightly warmer than 0°C (i.e., 0.0°–3.8°C). This situation is likely to lead to an overestimation of the retrieved LWP due to the following factors: 1) the melting snow accumulating on the radiometer radome and 2) the effect of scattering by rain, which has much larger drop sizes (>0.3 mm) than those of cloud droplets (Wei et al. 1989). Therefore, to

prevent contamination of the average LWP pattern up the slope, a quality check is performed in this section. Note that stringent criteria were proposed to reduce the likelihood of liquid water contamination (Murakami et al. 2000). However, in this study, those criteria were not applied because almost all of the LWP data in our case would be removed by them.

To remove raindrops and snow from the radome, the air blower was used. The air blower of the mobile radiometer was much less powerful than that of the Shimizu stationary radiometer (i.e., wind speed near the radome surface was about 24 m s^{-1} for the Shimizu stationary radiometer and 12 m s^{-1} for the mobile radiometer). Figure 3 shows the correlation diagram between the LWP data from the mobile radiometer used around the Shimizu site and the Shimizu stationary radiometer. Radiometers were spaced about 10 to 20 m apart. The correlation coefficient of 0.84 suggests that some ambiguity remains, but this figure also indicates that the LWP from the mobile radiometer would not be overestimated. For the scattering signals from the rain, we visually inspected the LWP time series and 2D-Grey particle images. The positions of the LWP spikes were found to be associated primarily with the locations of small raindrop images observed in the 2D-Grey data. Consequently, about 3% of all the LWP data were removed. Although the LWP increases with the distance up the slope, the likelihood of rain contamination decreases, therefore, the LWP measurements are actually more reliable where LWP values are greater up the slope.

b. The Ka-band Doppler radar

The Ka-band Doppler radar (Hamazu et al. 2003) was deployed at the upwind valley site of 290 m altitude on the Uonuma Hills. In this work, RHI scan data were used around the 141° azimuth with respect to the direction along the observation sites, the mobile measuring route, and the downwind direction from the radar site to the axis of the Shimizu Valley. Details on the radar specifications, scanning strategy, dealiasing method, and the effects of the hydrometeor and gaseous attenuation are given in KM04. Mie scattering by snowflakes of several millimeters can introduce an uncertainty into the reflectivity values (Gunn and East 1954). Since the median diameters of snow particles sampled by the mobile 2D-Grey probe are between about 1.0 and 2.5 mm, the measured value of dB effective reflectivity factor (Z_e) would be 1dB ~ 4dB less than those measured by the centimeter-wavelength radar (Matrosov 1998). The ice water path (IWP) data were calculated by vertically integrating the ice water contents (IWCs) derived from radar reflectivities over the bins above 200 m AGL. This domain had little influence from the ground clutter (see Fig. 9), which causes the overestimation of the IWP. As for KM04, the Z_e–IWC relation for Ka-band radar (Liao and Sassen 1994, hereafter LS94) is applied here to derive the IWCs. Variability in size spectra, densities, and shapes of snow particles lead to uncertainty in the IWC estimates from radar reflectivity. LS94's model was based on solid ice particles and they noted that low-density relatively large particles could be expected to have an influence on the radar reflectivity-versus-mass relation. The magnitude of IWC in this case is likely to be overestimated, however, this should not be a problem for this study, since we compare relative spatial distribution rather than absolute magnitudes.

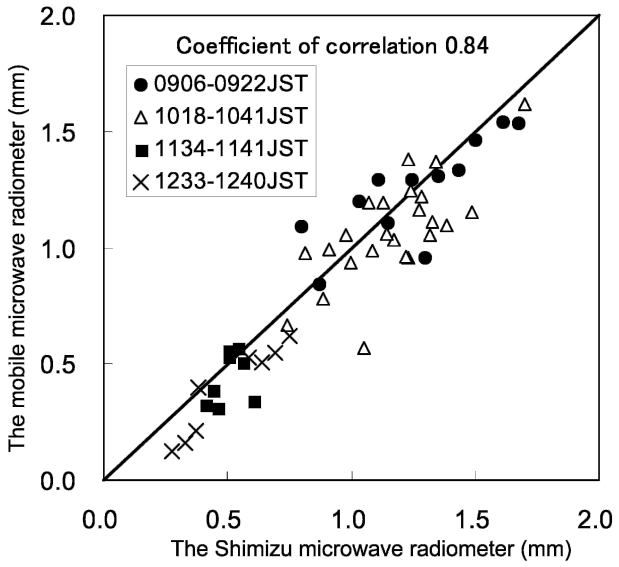

FIG. 3. Correlation diagram between the LWP data from the mobile radiometer and the Shimizu stationary radiometer.

3. Supercooled liquid water and snow particle distributions

During the study period, only quasi-stationary and shallow orographic clouds prevailed, and the typical echo was characterized by a stratiform with a weak embedded convection. The synoptic and environmental conditions are described in detail by KM04. The wind hodograph (Fig. 4) indicates that the wind speed increased with height, and the winds shifted northerly at the bottom of the Muikamachi Basin (hereafter BMB), but the mean wind direction was northwesterly, that is, along the valley axis. Figure 5 shows the spatial distributions of wind speed and direction, the LWP, the number concentration of snow particles, the precipitation rate, and the IWP. Precipitation rates were derived from 2D-Grey particle size spectra and the values of fall speed and density of snow particles. For estimating these values, particle types are roughly assumed to be heavily rimed dendrites (R3b) with a diameter below 3 mm and lump graupel (R4b) with a diameter above 3 mm (Rasmussen et al. 1999). The spatial distributions of these variables are obtained by averaging the data

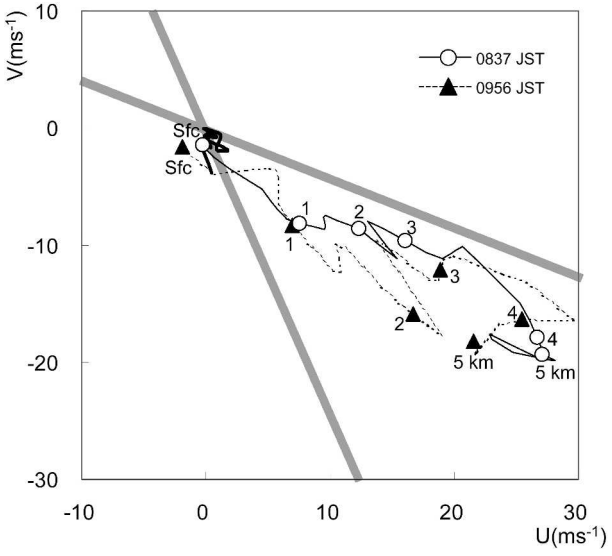

FIG. 4. Wind hodographs for 1737 (solid line with circles) and 1856 UTC (dashed line with triangles). Altitudes are shown on the curves. Profiles obtained with the mobile platform are superimposed (bold lines). Thick gray lines indicate the directions of the Shimizu Valley sidewalls.

from the mobile instruments and Ka-band radar. The mobile instrument data are averaged over the four round trips between 1742 and 2211 UTC. The radar data (reflectivity and Doppler velocity) are averaged over 23 RHI scans (1742–2156 UTC) around an azimuth of 141° from the direction along the valley axis.

Figure 5a shows the wind distributions observed with the mobile platform. The averaged Doppler velocities observed with the Ka-band radar are depicted in Fig. 5b. The radar beam was pointing at the azimuth angle of 141° and the elevation angle of 2°. The Doppler velocities of the radar beam can be assumed to represent the wind speed up the slope. Similar to the wind hodograph from the rawinsonde soundings (Fig. 4), the mobile wind directions (Fig. 5a) indicate that the winds shifted northerly at BMB, but the mean wind direction was northwesterly, that is, along the valley axis. The averaged Doppler velocity distribution (Fig. 5b) indicates that the wind speed increased with height. The wind speed at the mobile platform (Fig. 5a) exhibits a trend similar to that of the Ka-band radar, but is often enhanced by the local terrain forcing. Figure 1 indicates that the locations of the remarkably enhanced strong wind are associated with the bottleneck locations. One possibility for the wind enhancement may be the Venturi effect (i.e., the flow converges and, thereby, is accelerated between narrowing valley walls). Another one could be the hydraulic effect caused by a pressure gradient associated with the decreasing depth of cold air in the gap (Sharp and Mass 2002).

Figure 5c shows the LWP distribution observed with the mobile platform. Similar to the wind speed, the LWP is associated with terrain height. The orographic lifting due to the increase of the wind speed up the slope leads to the generation and increase of supercooled cloud droplets. The relationship between LWP and terrain slope can be shown to be particularly pronounced at small spatial scales by examining the LWP versus terrain height in a perturbation sense (Fig. 6). Concerning the terrain, the highest altitudes are indicated around the mobile platform route (i.e., approximately 1 km around its path), since the higher terrain on both sides of the road affects the airflow. In creating Fig. 6, the linear trend was removed, and the resulting perturbation field was smoothed with a 2.5-km running mean. Figure 6 indicates that there is a positive correlation between the two variables up the slope. Locally enhanced updrafts may exist where the airflows ascends over the abrupt terrain rises (~3 km horizontal scale), and such updrafts may generate supercooled cloud droplets. It is noteworthy that such small-scale terrain-induced SLW detectable by a microwave radiometer was also reported by Huggins (1995, see his Fig. 9) who, based on DRI MMR observations, documented the spatial characteristics of the cloud liquid over the Wasatch Plateau in central Utah. Over the Tushar Mountains of southwestern Utah (about 180 km south-southwest of the Wasatch Plateau), Sassen et al. (1990) also obtained a similar result by combining polarization lidar and scanning microwave radiometer observations. Such cloud liquid water associated with the smaller-scale uplift induced by topography was also demonstrated in high-resolution numerical models, for example, the Clark–Hall model (Bruintjes et al. 1994).

Figures 5d and 5e show the distributions of the total number concentration of snow particles and precipitation rates derived from the 2D-Grey measurements, respectively. Similar to the wind speed and LWP patterns, the number concentrations (0.1–6.4 mm in diameter) and precipitation rates are correlated with altitude. Figure 7 shows the number concentration for each particle size from the 2D-Grey measurements. This figure demonstrates that a greater concentration of large particles tends to appear over the windward slope but not over the BMB. Most of the 2D-Grey particle images exhibit quasi-circular shapes with rounded edges, suggesting significant riming (Fig. 8). It follows from Figs. 5d, 7, and 8 that ice crystals would grow by riming to become large snow particles at higher altitudes up the slope. The dips in Fig. 5d, which are also seen in Fig. 7, are associated with the abrupt terrain rises and indicate that the mobile platform path was locally sheltered from snow particles by the small-scale topographic barriers. These dips and the bottleneck effect described above are not discussed in detail here, since they do not affect relative variations in the averaged cloud properties examined in this study.

Figure 5f indicates that the IWP increases with terrain height, reaches the maximum intensity at 14 km up the slope, and then decreases. Figure 9 shows the averaged reflectivity pattern. This figure indicates that the

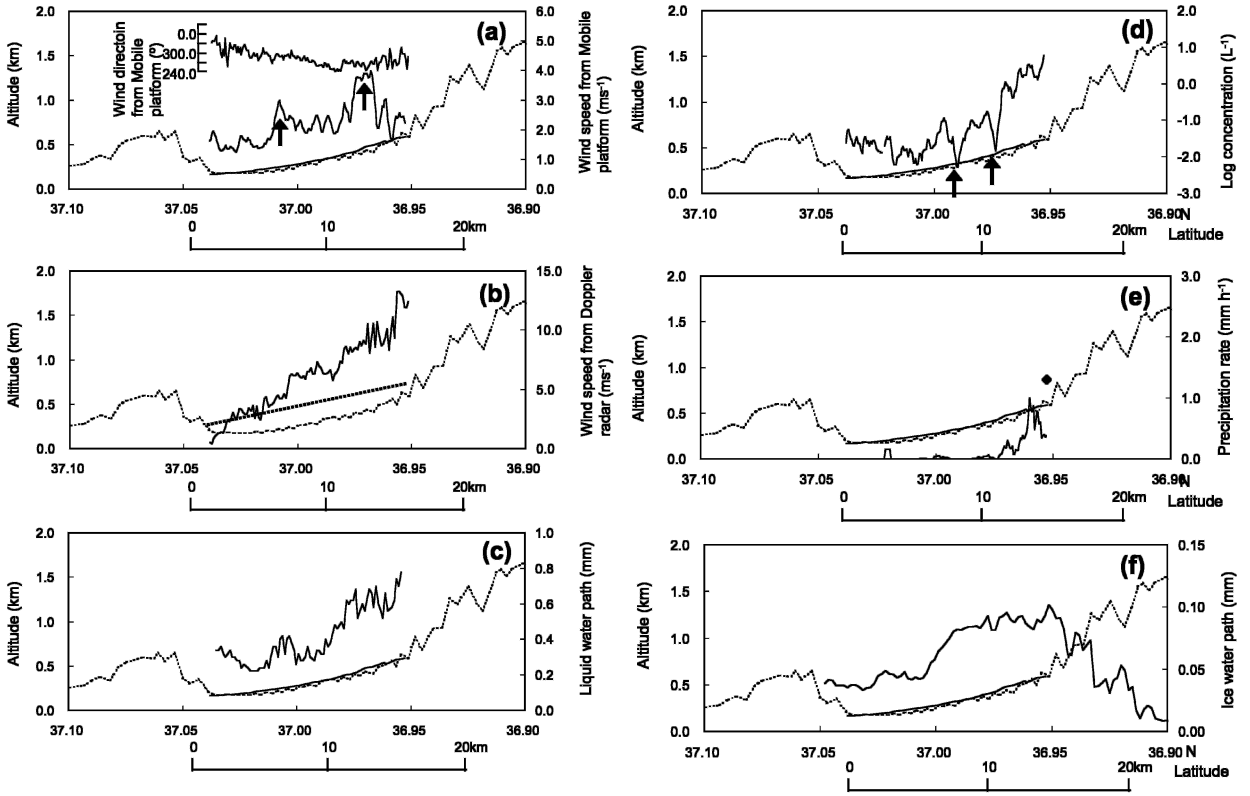

FIG. 5. Time-averaged distributions. The data are averaged over the four round trips between 1742 and 2211 UTC. The terrain heights along the azimuth angle 141° of the radar beam (dashed line) and along the mobile route (solid line) are superimposed. (a) The mobile platform wind speed and direction. The arrows indicate the locally enhanced wind speed. (b) Averaged Doppler velocity observed with the Ka-band radar (1732–2156 UTC). The radar beam (dotted line) pointing at the azimuth angle of 141° and elevation angle of 2°. (c) The LWP. (d) Total number concentration of particles. The arrows indicating the location of dips in number concentration associated with the sheltering effect can be clearly seen. (e) The precipitation rates, diamond indicates the averaged precipitation rate between 1700 and 2200 UTC from the rain gauge at the Shimizu site. (f) The IWP.

echo tops (−30 dBZ) were reached at about 2.5 km, and the relatively strong echo region (>−3 dBZ) appeared at 5 km up the slope and extended nearly parallel to the slope. The increase of the IWP and the relatively strong pattern reflects snow particle growth during the downwind advection and are consistent with the distribution of size and number of snow particles. The decrease in the IWP from the midbarrier comes from a decrease in the cloud thickness by increasing terrain height and nearly constant cloud-top height. Note that, although no mobile data were available beyond the Shimizu site, the LWP adjacent to the mountain ridge decreases for the same reason as the IWP.

Some of the 2D-Grey images in Fig. 8 indicate the existence of rimed dendrite particles. The average cloud-top temperature [from the high relative humidity (RH; >90%)] and the average echo-top temperature are −17° (KM04) and −13°C, respectively. Therefore, the upper cloud areas were more appropriate for dendritic ice-crystal growth. Actually, the hydrometer videosonde (HYVIS) observation upstream of the slope launched at 1856 UTC also indicates the distribution of dendrites (see Fig. 15 of KM04). Although there is no information on the vertical distribution of SLW up the slope, it is considered that primary ice nucleation near the top of the cloud is followed by deposition growth and aggregation of dendritic crystals. Low-level supercooled cloud droplets within the orographic updrafts

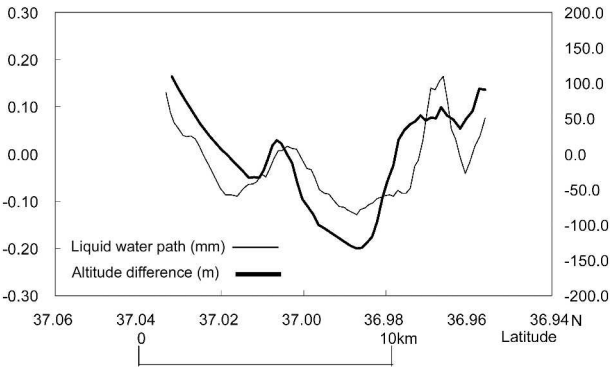

FIG. 6. Time-averaged perturbations of the terrain altitudes and the LWP 1742–2211 UTC. The linear trend was removed, and the resulting perturbation field was smoothed with a 2.5-km running mean.

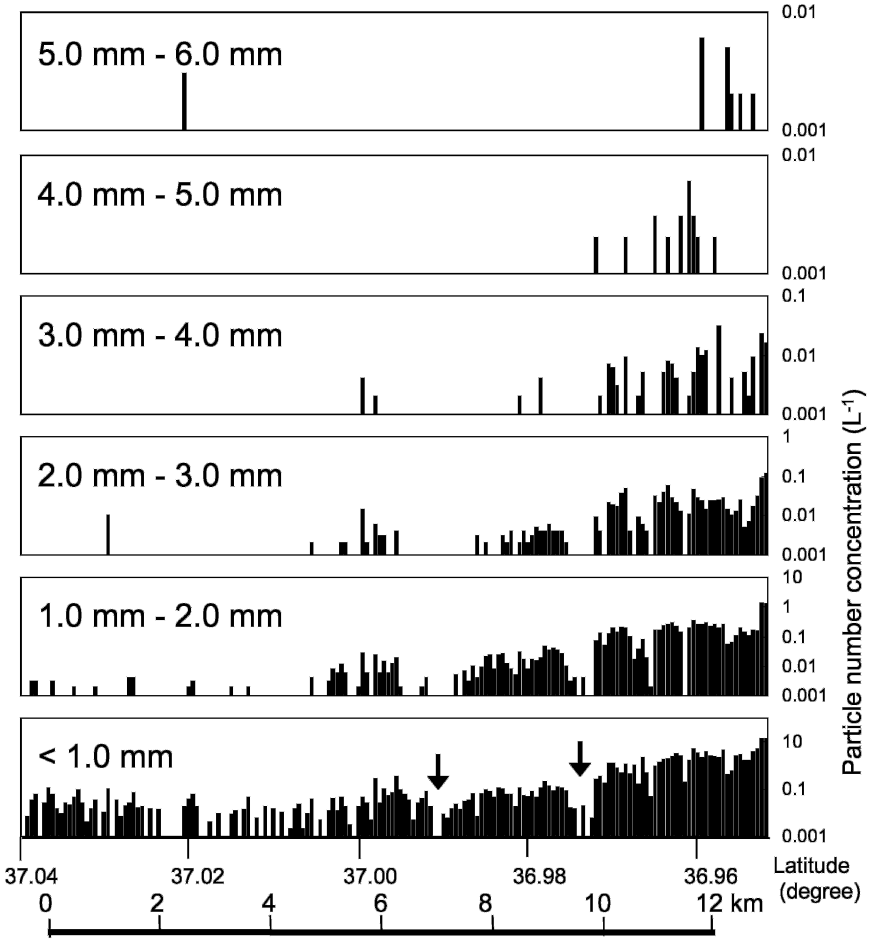

FIG. 7. The number concentrations for each particle diameter from the 2D-Grey measurements. The arrows indicate the locations at which the number concentration dips associated with a sheltering effect can be clearly seen.

may then be depleted by the descending ice particles from the cloud top. Support of this idea comes from the previous observational study of Rauber (1992), who showed a conceptual model of the precipitation process within the orographic storm observed in the course of the Sierra Cooperative Pilot Program (SCPP). He also reported that a cloud region near −5°C, which is appropriate for ice multiplication, was identified at the location where rising cloud droplets first encountered descending ice particles. Unlike his analysis, as we already noted in KM04, there was no evidence of ice multiplication in this case.

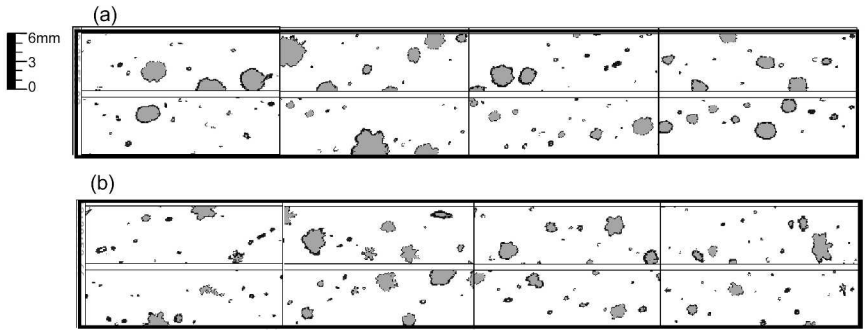

FIG. 8. Example of the 2D-Grey images measured around the Shimizu site: (a) 1825:55–1826:27 and (b) 2129:53–2130:16 UTC.

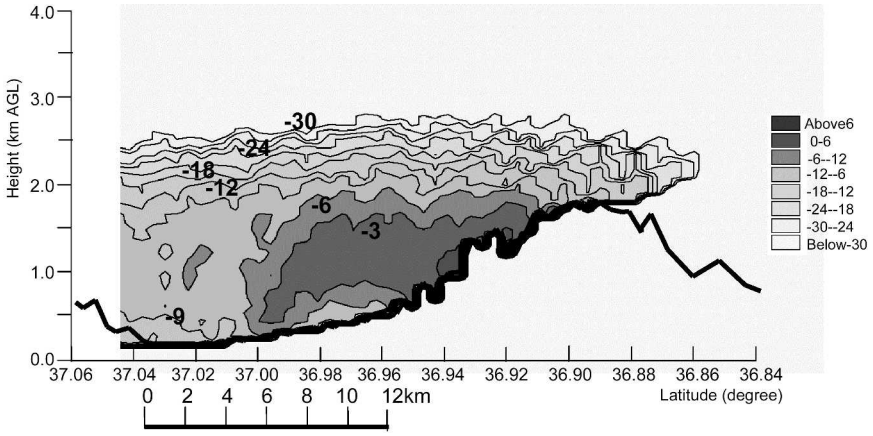

FIG. 9. The averaged reflectivity RHI scan at the azimuth angle 141° along the valley axis in Fig. 1. The data are averaged over 23 RHI scans (1732–2156 UTC). The terrain heights are superimposed. Note that the highest reflectivity near the surface between about 14 and 16 km downwind of BMB is due to ground clutter contamination.

4. Summary and conclusions

This paper examined the spatial distributions of the microphysical structures of the snow clouds over the windward slope by using a Ka-band Doppler radar and vehicle-mounted instruments, including a microwave radiometer and a 2D-Grey imaging probe. The spatial distributions of the LWP, number concentration of snow particles (0.1–6.4 mm diameter), and precipitation rates are correlated with altitude. Greater concentrations of larger particles tend to appear up the slope but not over the BMB. The echo tops were detected at about 2.5 km (-30 dBZ), and a relatively strong echo region (>-3 dBZ) was found at 5 km up the slope, extending farther downwind and up the slope. Reflecting the echo pattern, the IWP increases with terrain height and reaches maximum intensity at about 14 km up the slope. There is a positive correlation between small-scale terrain rises and LWP.

Although there is no information on the vertical structure of SLW or in-cloud hydrometeors up the slope, the present results are consistent with the hypothesis that is summarized in the schematic diagrams shown in Fig. 10. Downwind of the BMB, the orographic lifting leads to the generation and increase of supercooled cloud droplets due to the increase in the wind speed up the slope. Supercooled cloud droplets could be generated by locally enhanced updrafts over the small-scale (~3 km horizontal scale) terrain rises. Primary ice nucleation near the cloud top was followed by deposition growth and aggregation of dendritic crystals, and then the low-level supercooled cloud droplets within the orographic updrafts could have been depleted by descending ice particles from the cloud top. This riming process likely plays an important role for the snow particles that become larger at higher altitudes. A relatively strong echo region associated with a high concentration of larger particles, which extended nearly parallel to the slope, was formed.

In this paper, it is directly confirmed that the abundance of SLW during an intensified monsoon flow is due to the higher water production associated with

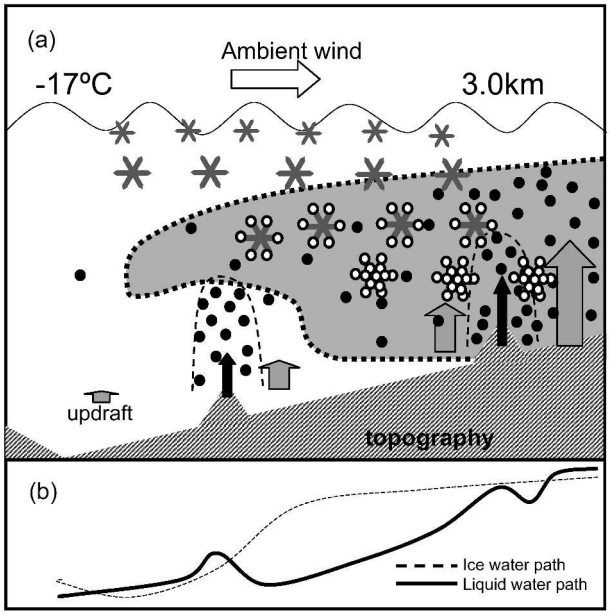

FIG. 10. Schematic of the spatial distribution of cloud droplets and snow particles in an orographic snow cloud and their relation to LWP and IWP. (a) The terrain (stripe shading), the updrafts associated with the slope (gray-shaded arrows), the locally enhanced updrafts (black arrows), the cloud droplets (black circles), the dendritic particles (asterisks), the rimed particles (asterisks with gray circles), the dense cloud regions associated with the locally enhanced updrafts (enclosed by thin dashed lines), the relatively strong echo region (shaded area enclosed by a bold dashed line), and the cloud top (wavy line). (b) The horizontal distributions of the LWP (solid line) and IWP (dashed line).

larger vertical velocities induced by the topography. Furthermore, small-scale terrains enhanced localized updrafts embedded within the larger-scale flow and had noticeable impacts on the SLW cloud distribution. The results of this paper, as well as those of KM04, provide a deeper understanding of the evolution of orographic snow clouds over the Japan Sea area and constitute a basis for future studies of storm modification by increasing precipitation. It should be emphasized that actual precipitation augmentation by cloud seeding depends on many additional factors including natural ice nucleation, growth, trajectories, and other microphysical processes. In this case study much SLW, indicating seeding potential, was found up the slope. However, it also appears that the cloud was naturally seeded with ice. Therefore, it is not clear whether the artificial seeding could make a difference for precipitation. More studies are required to quantitatively assess the precipitation augmentation potential.

Acknowledgments. This study is a part of the joint project of the orographic snow cloud modification by seeding which is conducted by Tone River Dams Integrated Control Office and the Meteorological Research Institute. The project is supported by the Ministry of Land, Infrastructure, and Transport of Japan.

REFERENCES

Bruintjes, R. T., T. L. Clark, and W. D. Hall, 1994: Interactions between topographic airflow and cloud/precipitation development during the passage of a winter storm in Arizona. *J. Atmos. Sci.,* **51,** 48–67.

Cooper, W. A., and C. P. R. Saunders, 1980: Winter storms over the San Juan Mountains. Part II: Microphysical processes. *J. Appl. Meteor.,* **19,** 927–941.

Deshler, T., 1988: Corrections of surface particle probe measurements for the effects of aspiration. *J. Atmos. Oceanic Technol.,* **5,** 547–560.

Gunn, L. S., and T. W. R. East, 1954: The microwave properties of precipitation particles. *Quart. J. Roy. Meteor. Soc.,* **80,** 522–545.

Hamazu, K., H. Hashiguchi, T. Wakayama, T. Matsuda, R. J. Doviak, and S. Fukao, 2003: A 35-GHz scanning Doppler radar for fog observations. *J. Atmos. Oceanic Technol.,* **20,** 972–986.

Heggli, M. F., L. Vardiman, R. E. Stewart, and A. Huggins, 1983: Supercooled liquid water and ice crystal distributions within Sierra Nevada winter storms. *J. Climate Appl. Meteor.,* **22,** 1875–1886.

Heymsfield, A. J., and J. L. Parrish, 1978: Techniques employed in the processing of particle size spectra and state parameter data obtained with the T-28 aircraft platform. National Center for Atmospheric Research Rep. NCAR/TN-137&A, 78 pp. [Available from NCAR, P.O. Box 3000, Boulder, CO 80307-3000.]

Hogg, D. C., F. O. Guiraud, J. B. Snider, M. T. Decker, and E. R. Westwater, 1983: A steerable dual-channel microwave radiometer for measurement of water vapor and liquid in the troposphere. *J. Climate Appl. Meteor.,* **22,** 789–806.

Holroyd, E. W., III, 1986: Surface sampling of a snowstorm by a 2D-C probe with and without aspiration. *J. Atmos. Oceanic Technol.,* **3,** 755–758.

Huggins, A. W., 1995: Mobile microwave radiometer observations: Spatial characteristics of supercooled cloud water and cloud seeding implications. *J. Appl. Meteor.,* **34,** 432–446.

Knollenberg, R. G., 1970: The optical array: An alternative to scattering or extinction for airborne particle size determination. *J. Appl. Meteor.,* **9,** 86–103.

Kusunoki, K., M. Murakami, M. Hoshimoto, N. Orikasa, Y. Yamada, H. Mizuno, K. Hamazu, and H. Watanabe, 2004: The characteristics and evolution of orographic snow clouds under weak cold advection. *Mon. Wea. Rev.,* **132,** 174–191.

Li, L., and J. W. Pomeroy, 1997: Estimates of threshold wind speeds for snow transport using meteorological data. *J. Appl. Meteor.,* **36,** 205–213.

Liao, L., and K. Sassen, 1994: Investigation of relationships between Ka-band radar reflectivity and ice and liquid water content. *Atmos. Res.,* **34,** 231–248.

Matrosov, S. Y., 1998: A dual-wavelength radar method to measure snowfall rate. *J. Appl. Meteor.,* **37,** 1510–1521.

Murakami, M., M. Hoshimoto, N. Orikasa, K. Kusunoki, and Y. Yamada, 2000: Microstructure and precipitation processes in a stable orographic snow cloud over the Mikuni Mountains in central Japan. Preprints, *13th Int. Conf. on Cloud and Precipitation,* Reno, NV, ICCP, 371–374.

Radiometrics, 1997: WVR-1100 Water Vapor and Liquid Water Radiometer. Radiometrics Corporation, 32 pp.

Rasmussen, R. M., J. Vivekanandan, and J. Cole, 1999: The estimation of snowfall rate using visibility. *J. Appl. Meteor.,* **38,** 1542–1563.

Rauber, R. M., 1992: Microphysical structure and evolution of a central Sierra Nevada shallow orographic cloud system. *J. Appl. Meteor.,* **31,** 3–24.

——, and L. O. Grant, 1986: The characteristics and distribution of cloud water over the mountains of northern Colorado during wintertime storms. Part II: Spatial distribution and microphysical characteristics. *J. Climate Appl. Meteor.,* **25,** 489–504.

Sassen, K., A. W. Huggins, A. B. Long, J. B. Snider, and R. J. Meitin, 1990: Investigations of a winter mountain storm in Utah. Part II: Mesoscale structure, supercooled liquid water development, and precipitation processes. *J. Atmos. Sci.,* **47,** 1323–1350.

Sharp, J., and C. Mass, 2002: Columbia Gorge gap flow. *Bull. Amer. Meteor. Soc.,* **83,** 1757–1762.

Wei, C., H. G. Leighton, and R. R. Rogers, 1989: A comparison of several radiometric methods of deducing path-integrated cloud liquid water. *J. Atmos. Oceanic Technol.,* **6,** 1001–1012.